Journal of Microbiological Methods 85 (2011) 67–74

Contents lists available at ScienceDirect

Journal of Microbiological Methods

journal homepage: www.elsevier.com/locate/jmicmeth

Ultrabright planar optodes for luminescence life-time based microscopic imaging of O_2 dynamics in biofilms

M. Staal [a], S.M. Borisov [b], L.F. Rickelt [a], I. Klimant [b], M. Kühl [a,c,*]

[a] Marine Biological Section, Department of Biology, University of Copenhagen, Strandpromenaden 5, DK-3000 Helsingør, Denmark
[b] Institute of Analytical Chemistry and Radiochemistry, Graz University of Technology, Stremayrgasse 16/III, 8010 Graz, Austria
[c] Plant Functional Biology and Climate Change Cluster, University of Technology Sydney, PO Box 123, Ultimo Sydney NSW 2007, Australia

ARTICLE INFO

Article history:
Received 7 December 2010
Received in revised form 17 January 2011
Accepted 18 January 2011
Available online 26 January 2011

Keywords:
Biofilm
Imaging
Luminescence
Microscopy
Oxygen
Optode

ABSTRACT

New transparent optodes for life-time based microscopic imaging of O_2 were developed by spin-coating a μm-thin layer of a highly luminescent cyclometalated iridium(III) coumarin complex in polystyrene onto glass cover slips. Compared to similar thin-film O_2 optodes based on a ruthenium(II) polypyridyl complex or a platinum(II) porphyrin, the new planar sensors have i) higher brightness allowing for much shorter exposure times and thus higher time resolution, ii) more homogeneous and smaller pixel to pixel variation over the sensor area resulting in less noisy O_2 images, and iii) a lower temperature dependency simplifying calibration procedures. We used the new optodes for microscopic imaging of the spatio-temporal O_2 dynamics at the base of heterotrophic biofilms in combination with confocal imaging of bacterial biomass and biofilm structure. This allowed us to directly link biomass distribution to O_2 distribution under both steady state and non-steady state conditions. We demonstrate that the O_2 dynamics in biofilms is governed by a complex interaction between biomass distribution, mass transfer and flow that cannot be directly inferred from structural information on biomass distribution alone.

1. Introduction

Molecular oxygen (O_2) is a key molecule for important biogeochemical and metabolic processes (Fenchel and Finlay, 2008; Glud, 2008). It is produced by oxygenic phototrophs (cyanobacteria, algae and plants) and is the preferred terminal electron acceptor in biological breakdown of carbohydrates since it generates the highest energy yield compared to other electron acceptors. Higher O_2 levels are critical e.g. for anaerobic microorganisms and processes, and for aerobic organisms due to formation of reactive oxygen species that can damage cellular processes. The O_2 distribution in biological systems can thus have strong effects on biogeochemical conversion rates and growth yields affecting the morphology of tissues and cell clusters. Local variations in O_2 respiration or production rates coupled with mass transfer limitations, e.g. due to the presence of diffusive boundary layers, can lead to steep spatial gradients of O_2 that respond dynamically to environmental parameters such as light or flow (Fenchel and Finlay, 2008). Oxygen concentration can vary strongly at μm to mm scale and precise quantification of the O_2 distribution and dynamics is a prerequisite for understanding the performance and regulation of many metabolic conversion rates, biotechnological and biomedical processes.

Oxygen dynamics can be monitored at high spatio-temporal resolution with electrochemical or fiber-optic O_2 microsensors (Klimant et al., 1995, 1997; Kühl, 2005; Revsbech, 2005). However, the spatial coverage is limited due to the one-dimensional nature of such measurements, and it is difficult to describe the spatial heterogeneity of systems with microsensor techniques, especially under non steady state conditions. With the development of planar optodes, a new tool for mapping the spatial distribution of O_2 became available (Glud et al., 1996; Kühl and Polerecky, 2008). Planar optodes use luminescent O_2 indicators immobilized in a polymeric matrix, which is permeable to O_2 and can be fixed on foils or glass surfaces. The measuring principle is based on the dynamic collisional quenching of the indicator luminescence by O_2 (DeGraff and Demas, 2005). Using sensitive gated CCD camera systems, O_2 dependent levels of luminescence and its exponential decay characteristics can be imaged, ultimately resulting in a description of the two dimensional distribution of O_2 (Holst et al., 1998; Liebsch et al., 2000; Oguri et al., 2006).

Hitherto planar O_2 optodes have mostly been based on the use of either ruthenium(II) polypyridyl complexes or metallo-porphyrines as O_2 indicators (Amao, 2003; Wolfbeiss, 2005). These indicators exhibit moderate luminescence brightness with luminescence life-times in the μs–ms range. Recently, novel optical sensor materials were developed, based on the use of cyclometalated iridium(III) coumarin complexes as O_2 indicators with an exceptionally bright luminescence (Borisov and Klimant, 2007; DeRosa et al., 2004). These

* Corresponding author at: Strandpromenaden 5, DK-3000 Helsingør, Denmark. Tel.: +45 35321956; fax: +45 35321951.
E-mail address: Mkuhl@bio.ku.dk (M. Kühl).

0167-7012/$ – see front matter © 2011 Elsevier B.V. All rights reserved.
doi:10.1016/j.mimet.2011.01.021

new O_2-sensitive dyes are suitable for application in ultrathin transparent sensor layers, enabling very short response times and spatial resolution at the single cell level. A thin layer and short response time are required e.g. when fast changes in O_2 concentrations under non steady state conditions are monitored.

Here we present new thin layer optodes based on the new iridium (III) coumarin complexes immobilized in a 1 µm thick layer on a microscope cover slip. We compare the O_2 measuring characteristics of the new optodes with other thin planar optodes based on ruthenium(II) polypyridyl and platinum(II) porphyrin complexes (Kühl et al., 2007) and apply the new optodes for combined microscopic imaging of biomass, O_2 dynamics and spatial gradients in heterotrophic microbial biofilms under different flow regimes.

2. Materials and methods

2.1. Optode preparation

Three different types of luminescent O_2 indicators were used in this study: i) ruthenium(II)-tris-4,7-diphenyl-1,10 phenantroline (Ru-DPP), ii) platinum(II)-meso-tetra(pentafluorophenyl)porphyrin (Pt-TFPP), and iii) iridium(III) acetylacetonato-bis(3-(benzothiazol-2-yl)-7-(diethylamino)-coumarin) (IrC). Ru-DPP and IrC were synthesized as described elsewhere (Klimant and Wolfbeiss, 1995; Borisov and Klimant, 2007). Pt-TFPP was obtained commercially (Frontier Scientific Inc., USA). All luminescent dyes were immobilized in the same polystyrene (PS) matrix (ST316310/1 LS223989 JV, Goodfellow Ltd., Cambridge, UK) to guarantee similar gas diffusion characteristics within the optode. Dye concentrations (mg indicator per g PS) were 18.75 mg Ru-DPP/g, 25 mg Pt-TFPP/g, and 15 mg IrC/g. Thin-film optodes were fabricated by spin coating ~1 µm thick indicator layers onto 20×50 mm silanized microscope coverslips (Kühl et al., 2007).

2.2. Optode calibration setup

Optodes were calibrated at 20 °C in freshwater with defined O_2 concentrations. The optodes were placed in a holder on the window of a small water filled tank. The temperature of the tank was controlled by a cryostat (Julabo F25 HD, Germany). Oxygen levels in the calibration chamber were varied by flushing the water with defined gas mixtures of N_2 and O_2 at a flow rate of 0.6 l min^{-1}. Mixtures were generated with a PC-controlled programmable gas mixing system using electronic mass flow controllers (Sensorsense, Netherlands). The O_2 concentration in the water was increased step wise, at time intervals including at least 2 min of steady state at each O_2 concentration. Additionally, O_2 levels in the water were monitored with a fiber-optic O_2 minisensor system (Fibox 3, Presense GmbH, Germany). The temperature dependence of the planar sensor luminescence was measured at two different O_2 concentrations in steps of 5 °C over a range of 5–30 °C.

2.3. Life-time imaging system and image calibration

Luminescence life-time and intensity of the optodes was imaged with a modular luminescence life-time imaging system (Holst et al., 1998) consisting of i) a fast gate-able 12 bit SVGA CCD (1280×1024 pixel) camera (SENSICAM-SENSIMOD, PCO AG, Germany) equipped with a macro lens (Xenoplan XNP 1.4/17, Schneider-Kreutznach, Germany) and a 590 nm (30 nm bandwidth) bandpass filter, ii) a custom built trigger box driving two high power blue LED's (1 W Luxeon Star, 470 nm, Lumileds) for the excitation of the Ru-DPP and IrC optodes, or two UV power LED's (405 nm 1 W, Roithner Lasertechnik GmbH, Austria) for excitation of the Pt-TFFP optode, and iii) a custom-built PC-controlled pulse-delay generator. Image acquisition and hardware control were done with a custom made software program (Holst and Grunwald, 2001).

Life-time imaging with the system was done by acquiring luminescence intensity images (using a binning of 2), within two different time windows, w1 and w2, after the eclipse of an excitation light pulse. The luminescence life-time (τ) was calculated as (Gerritsen et al., 1997):

$$\tau = \frac{\Delta t}{\ln(I_{w1}/I_{w2})} \quad (1)$$

where Δt is the time delay between the start time of recording of the two time windows, and I_{w1} and I_{w2} are the corresponding luminescence images.

Since the three O_2 indicator dyes have different light absorption and life-time characteristics, we optimized the measuring protocols for each dye. In this study, we used excitation light pulses of 5, 5 and 7 µs for Ru-DPP, IrC and the Pt-TFPP optodes, respectively. Two luminescence intensity images (I_{w1} and I_{w2}) were acquired over 3 µs. Image one (I_{w1}) was acquired at 0.1 µs while the second image (I_{w2}) was acquired at 3.1 (Ru-DPP), 4.1 (IrC) or 7.1 µs (Pt-TFPP) after the excitation light pulse. These measurements were repeated and image pixel values integrated on the CCD chip over an exposure time period up to 400 ms to improve the signal to noise ratio. The first intensity window image is acquired by accumulation of Iw1 pulses over the integration time, and then the same is done for the second intensity window image. In this study we used exposure times of 100, 300 and 400 ms for IrC, Ru-DPP and Pt-TFPP optodes, respectively. Different exposure times were necessary to achieve comparable pixel intensity values on the camera, i.e., to obtain minimum grey values of >400 after subtraction of a dark image.

Image analysis was done in the custom made software *Look@-MOLLIdata* (Polerecky, http://www.mpi-bremen.de/Binaries/Binary4997/Polerecky-EADS-report-2005.pdf) and the freeware *ImageJ* (http://rsbweb.nih.gov/ij/). We analysed randomly selected regions of interest (ROI's) ($n = 6–10$) in the acquired images, each containing ~5000 pixels; regions at the very sensor edge or in the unevenly illuminated periphery of the field of view were avoided. From the ROI's we derived the average luminescence intensity (pixel value) of image 1 and image 2, as well as the average life-time and its standard deviation. Stern–Volmer plots of the data were fitted with a modified

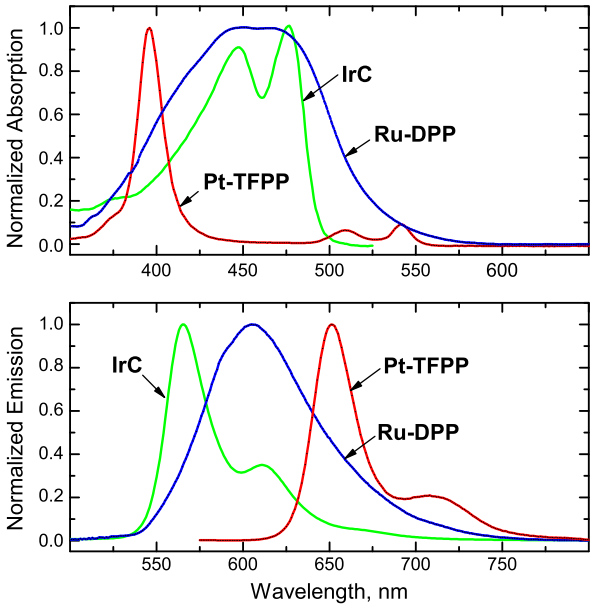

Fig. 1. Absorption and luminescence emission spectra of optical O_2 indicators immobilized in polystyrene: ruthenium(II)-tris-4,7-diphenyl-1,10 phenantroline (Ru-DPP), platinum(II)-meso-tetra(pentafluorophenyl)porphyrin (Pt-TFPP), and iridium(III) acetylacetonato-bis(3-(benzothiazol-2-yl)-7-(diethylamino)-coumarin) (IrC).

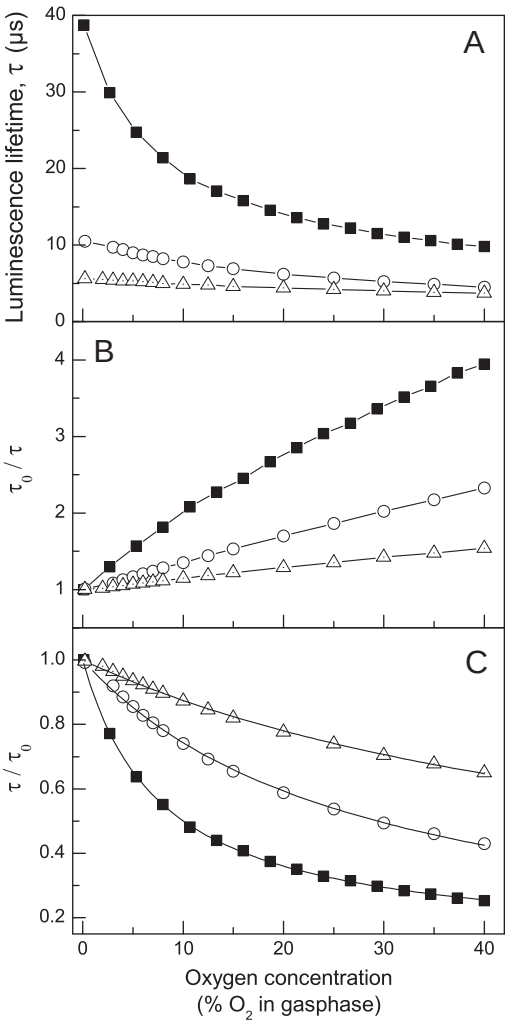

Fig. 2. Luminescence life-time (τ) vs. O_2 concentration (A) and corresponding Stern–Volmer relationship (B) measured at 20 °C for the Pt-TFPP (black squares), IrC (open circles) and Ru-DPP (open triangles) optodes. C. Inverse of Stern–Volmer relationship with O_2, including curve fits estimating α and K_{sv}.

Stern–Volmer equation that accounts for a non quenchable fraction, α, within the optode (Carraway et al., 1991):

$$\frac{I}{I_0} = \frac{\tau}{\tau_0} = \frac{1-\alpha}{I + K_{sv}C} + \alpha \qquad (2)$$

where I_0 and I are the luminescence intensities at anoxia and in the presence of O_2 at concentration C, and τ_0 and τ are the equivalent luminescence life-times, α is the non-quenchable fraction within the sensor matrix, and K_{sv} is the quenching coefficient. Both K_{sv} and α were fitted from the τ/τ_0 vs. O_2 concentration curves using a non-linear fitting routine (Origin 7.5, OriginLab Corp, USA).

2.4. Microscopic O_2 imaging set up

Microscopic luminescence life-time imaging was done on an Olympus BX50W1 fixed stage microscope equipped with 40× and 60× water immersion objectives (Plan-Apo WLSM/40×, NA 0.9; Uplan-ApoW/60×; NA 1.20, Olympus, Japan). The imaging system was the same as described above, except that the CCD camera was mounted on the microscope via a C-mount, and a blue LED (5 W Luxeon star, 470 nm, Lumileds) was mounted in the epifluorescence port of the microscope (more details in Kühl et al., 2007).

Since light capturing was very efficient by the high NA microscope objectives, the integration time per intensity image was only 20 ms (I_{w1}, I_{w2} and I_{dark}). Maximal sampling rate was 1 life-time image per 1.5 s. The highest sampling rate applied in this study was one O_2 distribution image per 3 s. The same CCD camera was also used to acquire bright field images of biomass distribution, in order to allow direct comparison of the biomass pictures with the O_2 distribution images.

After the O_2 measurements, the biofilm was stained with a red fluorescent nucleic acid stain (Syto® 60, Molecular Probes, Inc., Eugene, OR). A spinning disk confocal imaging system (Ultraview LCI, Perkin Elmer) mounted on the same microscope (Kühl et al., 2007) was used to acquire stacks of optical sections through the biofilm (using laser excitation at 647 nm and collecting emission from the Syto 60 dye at >700 nm). The CCD camera used for confocal image detection had 1344×1024 pixels (Hamamatsu ORCA ER, Hamamatsu Photonics Inc., Japan).

There was only little overlap between the emission spectra of the IrC optode and the Syto 60 dye (max excitation/emission 652/678 nm; http://probes.invitrogen.com/media/pis/td11341.pdf). However, due to the high amount of IrC in the planar optode relative to the Syto 60 staining of the biofilm, there was significant luminescence detected from the optode when we measured the biomass with the confocal microscope close to the biofilm base. The first surface image in the biomass image stack was therefore affected by the optode and was excluded from the biomass reconstruction.

All image treatment was performed in *Image J* (freely available at http://rsbweb.nih.gov/ij/). Image handling comprised background correction, multiplication with a flat field correction image and summation of the resulting image stack as a proxy for biomass distribution. Since the confocal imaging and life-time imaging were not made with the same camera, and the resolution of the life-time images and the biomass images were not equal, the pixel size of the latter was reduced to the size of the life-time image. After resizing, the contours of the structures were determined by simple thresholding, and these contours were pasted into the life-time images. In addition, profile plots of the biomass images were extracted along the same lines as O_2 concentration profile plots extracted from O_2 images to enable comparison of biomass distribution and O_2 distribution.

2.5. Biofilm growth

Biofilms of heterotrophic bacteria were grown in small flow cells (Pamp et al., 2009; Stovall Life Science Inc, USA) with the glass cover replaced by an IrC thin-film optode glued to the flow cell with UV-curing adhesive (Adhesive 426, Light Welder PC-3; Dymax Europe GmbH, Germany). Each lane in the growth chamber was 4 cm long, 4 mm wide and 1 mm deep. A biofilm inoculum was grown from a sediment sample incubated in an aerated carbon rich medium containing basic nutrients (0.01 $g\,l^{-1}$ phosphate, 0.001 $g\,l^{-1}$ magnesium, 0.1 $g\,l^{-1}$ glucose, 0.1 $g\,l^{-1}$ Ca-acetate and 0.1 $g\,l^{-1}$ Na-succinate). The inoculum was flushed through the flow chamber at low flow (1 $ml\,h^{-1}$) to allow initial attachment of bacteria to the optode surface. Thereafter, new medium was continuously pumped through the flow chamber (flow rate 4 $ml\,h^{-1}$, resulting in a flow of 1 $m\,h^{-1}$ and a retention time of 2.4 min) with an adjustable high precision peristaltic pump (Minipulse 3, Gilson, France) to select for biofilm forming organisms. At these rates, flow in this type of biofilm growth chamber is laminar (cf. Pamp et al., 2009). Visible biofilm structures formed within 5 days. All tubing's (made of O_2 impermeable Tygon tubing) were replaced and fresh aerated medium was prepared prior to actual measurements to prevent substrate and O_2 consumption before the medium reached the incubation chamber. During the flow experiments, the retention time of the medium varied from 2 s at the highest flow to 7 min at the lowest flow rate.

3. Results

3.1. Measuring characteristics of thin-film optodes

The absorption maxima of the IrC and Ru-DPP optodes are in the blue spectral region, while thePt-TFPP optode has its highest absorption in the UV region (Fig. 1). The luminescence emission maxima are 565 nm, 605 nm and 650 nm for IrC, Ru-DPP and Pt-TFPP optodes, respectively. The new IrC-based planar optodes showed a three times higher brightness than Ru-DPP-based optodes for the same blue light excitation intensity, and in order to acquire images at similar pixel values, we used a three times longer integration time per image for the Ru-DPP optode (100 vs. 300 ms). To reach similar pixel values in measurements with the Pt-TFPP optode we used an integration time of 400 ms. However, the latter was partly due to the use of different LED's (405 nm) with a less focused emission characteristic.

There was a large difference in luminescence life-time between the three tested optodes (Fig. 2). At 20 °C, the Pt-FTTP optode had life-times ranging from 11 to 39 μs, IrC had life-times between 4.5 and 10.6 μs, while Ru-DPP had life-times between 3.7 and 5.5 μs, respectively, at 0 to 35% O_2 in the gas phase. The IrC optodes exhibited an almost Stern–Volmer relationship. Fitting the inverse of the Stern–Volmer curve showed that newly prepared IrC optodes exhibited a quasi ideal Stern–Volmer relationship following Eq. (2) with an α value close to zero, i.e. $\alpha = 0.02 \pm 0.03$ (mean ± standard deviation). Ru-DPP and Pt-FTTP had higher α-values of 0.11 ± 0.05 (mean ± standard deviation).

All optodes showed decreasing luminescence life-times with increasing temperature (SFig 1, 2). Under anoxic conditions, the τ_0 values of IrC, Pt-TFPP and Ru-DPP optodes showed a decreased in luminescence life-time of 3%, 7% and 7%, respectively, when temperature increased from 10 °C to 30 °C. The temperature effect was larger at 20% O_2, where τ values of IrC, Pt-TFPP and Ru-DPP optodes decreased 10%, 11% and 17%, respectively, over the same temperature range. Similar results were found by linear fitting of normalized τ values (STable 1, SFig. 2).

Old IrC optode kept over several months exhibited a reduction in τ_0 and an increase in the non-quenchable fraction, α (SFig. 3). Similar aging effects were found for the Ru-DPP optode (data not shown).

3.2. Sensor homogeneity

The O_2 distribution in the aquarium used for calibration measurements can be considered homogeneous, since the water was well mixed, no organic substrate was present and the optodes were carefully cleaned using a soft cotton stick and brief cleaning with 70% ethanol prior to the calibrations. Thus any spatio-temporal variation in luminescence life-time at a given constant O_2 level was caused by noise and optical artifacts in the camera system or inhomogeneities in the optode. The standard deviation of pixel values in the analyzed ROI's (~5000 pixels) was used as a proxy for homogeneity of the optode. Standard deviations within the obtained life-time images were analyzed at different O_2 concentrations. For all three optode types, the standard deviation of luminescence life-time values decreased with increasing O_2 concentration. Absolute standard deviations were highest for the Pt-TFPP optodes and ranged from 1.3 (high O_2) to 4 μs (anoxia), while the IrC optode had the lowest standard deviations varying from 0.1 to 0.4 μs. Since the luminescence life-time values depend on the O_2 concentration as well as the indicator type, the standard deviation was also expressed as percentage of the life-time. When expressed as percentage, there was less effect of the O_2 concentration on the standard deviation. The relative standard deviation of the luminescent life-time was again lowest for the IrC optode, followed by the Ru-DPP optode and the Pt-TFPP optode (STable 1). Thus, IrC optodes exhibited the best homogeneity in O_2 sensing within ROI's used for the calibration curve. An example of the homogeneity of luminescence intensity and life-time of all three types of optodes is shown in SFig. 4A.

Luminescence measurements with a scanning confocal microscope equipped with a 60× lens, showed a significantly better microscopic homogeneity of IrC optodes in comparison to Ru-DPP optodes (Fig. 4B). We did not have a laser line available to measure the

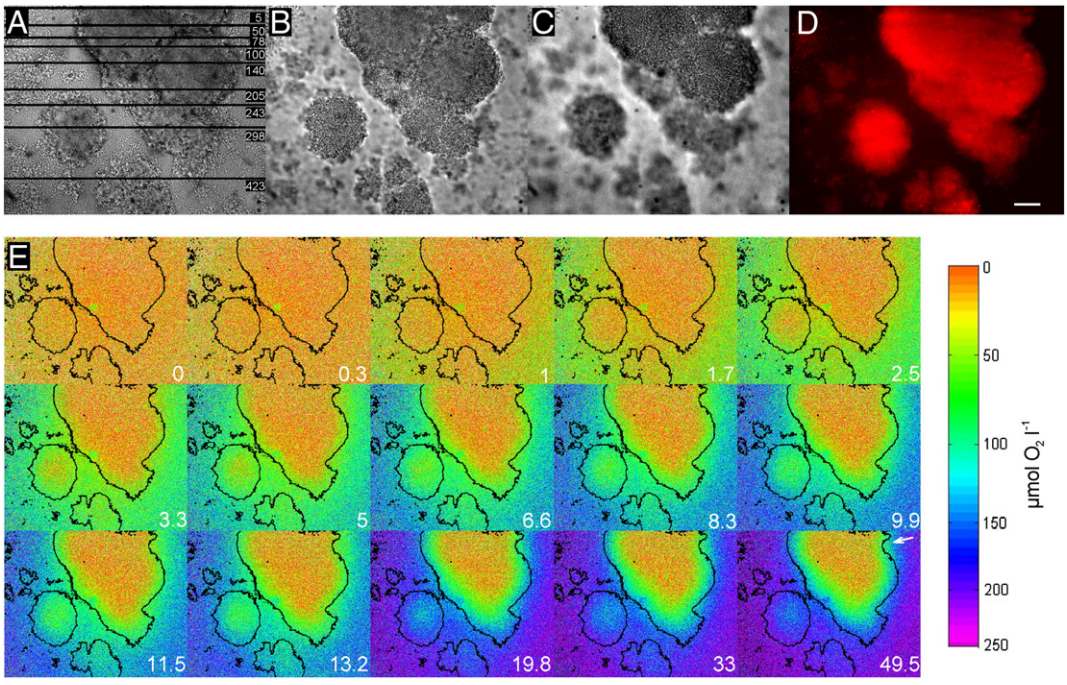

Fig. 3. Light transmission microscope images (A–C) of the biomass distribution in an ~25 μm thick heterotrophic biofilm grown on an IrC optode; images are focused on the base (A), central (B) and top (C) parts of the biofilm. Lines in the upper panel indicate where O_2 profiles were extracted (see Fig. 4). D. Maximal intensity projection image of a confocal fluorescence image stack of the Syto-60 stained biofilm. The image is false colored, where red indicates a high biomass. Scale bar indicates 10 μm. E. Montage of different O_2 distribution images in the same biofilm at different flow rates. Flow rates (m h^{-1}) are indicated in the lower right corner of panels. Black contours are inserted to indicate conspicuous biomass structures. The white arrow in the high flow image indicates an area with larger mass transfer resistance outside the biofilm structure.

heterogeneity of the Pt-TFPP optode, but macroscopic measurements clearly showed pixel heterogeneity in the luminescence image of the Pt-TFPP, which were not caused by the camera system.

3.3. Microscopic O_2 measurements in biofilms

Heterotrophic biofilms were grown on the surface of IrC thin-film optodes. Due to the high brightness of IrC and efficient light capture with the high NA objectives, microscopic O_2 imaging could be performed at a much lower integration time than in macroscopic imaging. At 400× magnification, O_2 was measured with a horizontal optical resolution of 0.16 µm per pixel.

The biofilms had a maximum thickness of ~25–30 µm and showed distinctive structures resulting in a heterogeneous distribution of biomass and O_2 concentration. Fig. 3A–D shows a ~50 µm wide and ~80 µm long cell aggregate together with two smaller ~25–30 µm wide cell clusters under the main structure with a thickness of ~15–20 µm. The same thickness was found for a part (lower half in the image) of the large aggregate. The three structures were separated by a channel like structure.

The O_2 conditions in the biofilm were strongly affected by the medium flow rate. The whole flow chamber became anoxic under stagnant conditions, while a more heterogeneous O_2 distribution was induced by higher flow rates (>5 m h^{-1}) (Fig. 3E). In areas with no or very thin biofilms (up to 5 µm thickness) O_2 levels increased with an increase in the flow rate. Pronounced O_2 gradients were found at the edges of thicker biofilm structures, especially at high flow rates (>10 m h^{-1}). The inner compartments of thicker biofilm parts remained anoxic, even at the highest flow rates, indicating that the O_2 demand of these structures was higher than the maximum potential O_2 influx.

The flow direction of the medium was from the top in the shown images, alleviating mass transfer limitation upstream of larger cell aggregates and increasing such limitations downstream. The gradient outside the black lines in Fig. 3 shows that on the upper left side of the major structure there is a very thin and steep O_2 gradient (2–3 µm) where the flow hits the structure. In contrast, in less flow exposed cavities of the biofilm on the upper right side of the major structure (indicated by a white arrow in the 49.5 m h^{-1} frame, Fig. 3), the O_2 concentration already decreased significantly outside the biofilm structure. There was also a shading effect visible in the channel in between the three larger biofilm structures, though some biomass was detected on the optode in that region, which may also explain the lower O_2 concentration.

After correction for image size and shifts due to the use of two different cameras it was possible to align biomass and O_2 distribution. In total, 9 horizontal lines (5 pixels thick) were analyzed, in order to visualize the relationship between biomass and O_2 distribution (Fig. 4) at two different flow rates. At low flow rate (4 m h^{-1}) the O_2 levels at the biofilm base was much lower than at high flow rate (30 m h^{-1}). We found no direct relationship between biomass on top of the optode and the O_2 concentration at the optode. Oxygen concentrations decreased already in regions surrounding the biomass structures due to mass transfer limitation. Furthermore, O_2 levels below larger cell aggregates remained anoxic despite a lower biomass in these regions (see Fig. 3 and the biomass indication lines in the graphs of line 5, 50, 78 and 100 in Fig. 4). At high flow, O_2 was able to penetrate all the way to the biofilm base in the thinner regions of the largest cell aggregate (Fig. 4, line 205, 243 and 298) alleviating anoxia. The width of the large structure was almost equivalent to the O_2 penetration depth from the side, i.e. maximally 15–20 µm at high flow rates and 8–14 µm at low flow rates (Fig. 4, line 5–140).

The measurements described above were performed under steady state conditions with a low temporal resolution (one sample per minute). Additional measurements at higher time resolution (one sample per 3 s) showed a more complex O_2 dynamics (Fig. 5). At the start of the experiment, the system was in steady state with no flow. At t = 0, the flow was turned on to maximum flow rate (70 m h^{-1}) and O_2 concentrations reached their maximum values within 10 s. For clarity we only show O_2 dynamics and biomass data (Fig. 5A, B) from line 50 (Fig. 3). The O_2 concentrations remained at maximal levels for the whole flow period outside large structures. Within the structures there was a decrease in O_2 concentration over time, especially in the zones (~10 µm from the aggregate edge) proximate to the anoxic part of the biofilm. The central parts of aggregates also remained anoxic during this experiment. Different O_2 depletion rates are found in the big aggregate structures (Fig. 5C). Fastest O_2 depletion (indicated with white arrows) was found in the peripheral parts of larger cell aggregates reaching rates of up to ~0.5 µmol O_2 l^{-1} s^{-1}. After 48 s the flow was turned off again, causing an immediate decrease in O_2 concentration.

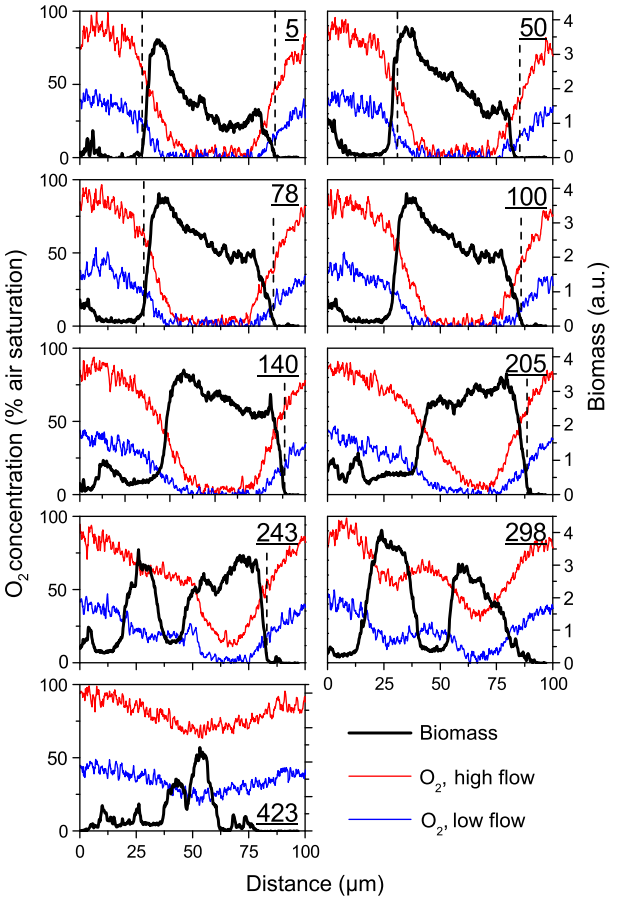

Fig. 4. Oxygen concentrations extracted from biofilm O_2 images obtained under high flow (red curves) and low flow (blue curves) conditions, respectively, along the pixel lines shown in Fig. 3. Numbers in each panel denote the pixel lines (y) in Fig. 3. The black line indicates the relative biomass in the biofilm as determined from confocal image stacks. Vertical dotted lines represent the edge of the biomass on the optode.

4. Discussion

Thin-film planar O_2 optodes are highly transparent and well suited for O_2 imaging combined with structural analysis of biofilms using light or confocal microscopy (Kühl et al., 2007). The new IrC-based optodes were superior to earlier developed Ru-DPP and Pt-TFPP based optodes in terms of a significantly higher brightness, better homogeneity of luminescence life-time images and thus less noisy O_2 images. IrC-based optodes also exhibited a lower temperature dependency of the O_2-dependent luminescence. The dynamic range of the

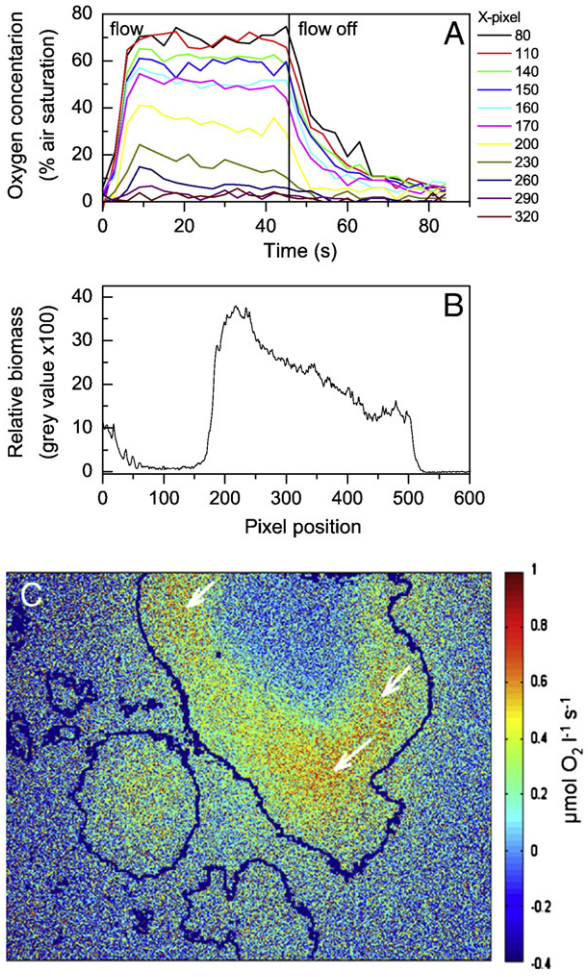

Fig. 5. A. Oxygen dynamics under non-steady state conditions at particular positions in the biofilm (distance between points is 10 pixels, i.e. 1.6 µm) on the horizontal line on pixel line 50 (see Fig. 3). Each point denotes an average of 5×5 pixels. The upper 3 lines (x-pixel 80, 110 and 140) represent positions in the area outside of the biofilm. Pixel position 280 represents the permanent anoxic zone, while positions in between pixel 140 and 290 represent a transient zone. At t = 0 the flow was turned on at 70 m h^{-1}, and flow was stopped again at t = 48 s. B. Biomass distribution in the investigated biofilm region. C. Image of O_2 depletion rate distribution in the biofilm calculated for the period between t = 12 s and t = 45 s. White arrows indicate zones with the strongest decrease in O_2.

luminescence life-time for the IrC optode falls in between Pt-TFPP and Ru-DPP based optodes, which makes the IrC optode suitable for O_2 imaging ranging from anoxic conditions up to about 2.5 times atmospheric saturation. The new IrC-based optodes enabled microscopic imaging of complex patterns in the spatio-temporal distribution of O_2 in biofilms that could be related to flow conditions and biomass distribution at a hitherto unreached resolution. In the following we discuss the measuring characteristics and biofilm application in more detail.

4.1. Heterogeneity effects

Despite the fact that luminescence life-time imaging corrects for heterogeneity in dye distribution, both Ru-DPP and Pt-TFPP based optodes exhibited relative high standard deviations in their life-time values (STable 1) reducing the operational spatial resolution of microscopic O_2 imaging as compared to IrC based optodes. It was reported that platinum porphyrin based optodes had a higher spatial resolution than ruthenium based optodes (Oguri et al., 2006). However, when expressing the standard deviations as percentage of total lifetime, as has been done in this study, the authors found a similar standard deviation with ruthenium and porphyrin based optodes (K. Oguri, personal communication).

A comparison of the thin-film optodes at higher (600×) optical magnification showed a higher heterogeneity of luminescence in the Ru-DPP optode than in the IrC-based optode. In a recent review (DeGraff and Demas, 2005), heterogeneity in O_2 optodes was attributed to i) macroheterogeneity in sensor materials due to non-optimal fabrication, ii) microheterogeneity due to phase separation and microcrystallization of the matrix polymer and/or the indicator dye, and e.g. microscopic cracks in the sensor material, and iii) nanoheterogeneity due to heterogeneity in molecular orientation and polymer nanostructure causing variations in O_2 diffusion and solubility. All these types of heterogeneity affect sensor response and can lead to a non-ideal Stern–Volmer quenching behavior, i.e. non-linear Stern–Volmer plots.

The spin-coating technique used in our study enabled fabrication of <1–2 µm thick homogeneous layers on glass coverslips that exhibited no significant macro heterogeneities (Kühl et al., 2007). However, our microscopic investigation (SFig. 4) showed pronounced microheterogeneities supporting earlier observations on Ru-DPP and Pt-porphyrin based optodes (Bedlek-Anslow et al., 2000; DeGraff and Demas, 2005; Eaton et al., 2004). A detailed discussion of mechanisms causing such heterogeneity and their effects on sensor performance is outside the scope of this paper. While micro- and possibly nano-heterogeneity was present also in the new IrC optodes, it was significantly lower than in Ru-DPP based optodes.

4.2. Bleaching and aging of optodes

Over longer times, i.e. months, the new IrC optode exhibited a decrease in luminescence life-time at all O_2 concentrations. In addition, it was found that the non quenchable fraction, α, increased from virtually zero in freshly prepared IrC optodes to 0.18 in 16 months old IrC optodes (SFig. 3). This increase could be caused by aging of the indicator/polymer matrix developing larger micro- and nano-heterogeneity (see above). However, an additional experiment showed that bleaching could reproduce the same effect on the life-time and the non-quenchable fraction within the IrC optode as aging (SFig. 3). Borisov and Klimant (2007) found that the IrC complex was easily bleachable upon illumination with a Xe light source. In our study we did not find a strong bleaching induced decrease in luminescence upon exposure to light from blue LED's or a halogen lamp. However, prolonged exposure to 488 nm laser light on the confocal microscope resulted in strong bleaching of the IrC as well as the Ru-DPP optode, which could be an important problem for using such indicators for more continuous luminescence intensity or ratiometric imaging on laser confocal microscopes. Microscopic luminescence life-time imaging measurements with the optodes used a blue 5 W power LED (470 nm) and we did not find any decrease in luminescence intensity measured over time under a permanent anoxic area, even after 250 consecutive O_2 measurements and several minutes exposure to the halogen lamp of the microscope. Thus, the new IrC optodes are well suited for luminescence life-time based microscopic imaging of O_2.

4.3. Response time and temperature effects

Luminescence signals from thin-film optodes are much lower than from conventional optodes using the same dye concentration. Conventional planar optodes have a thickness of 10–40 µm (Kühl and Polerecky, 2008), and the response time of such optodes is dependent on the equilibration time of the whole luminescent layer upon changes in O_2. This limits the temporal resolution when imaging fast O_2 dynamics, e.g. in studies of photosynthesis (Glud et al., 1999). Thin-film optodes have a much faster response time but may suffer from low luminescence. However, due to the high brightness of the

IrC-based optode it was possible to reduce the integration time by a factor of 3 in comparison to Ru-DPP and Pt-TFPP based thin-film optodes thus allowing a much higher temporal resolution. The temperature effect on the luminescence life-time was also smallest for the IrC optodes allowing measurements over a broader temperature range without the necessity to recalibrate the optode. This is especially convenient when O_2 is measured in phototrophic systems, since supplied light can heat surfaces locally (Jimenez et al., 2008).

4.4. Overall comparison of the O_2 optodes

All three types of O_2 optodes are capable of sensing the spatio-temporal dynamics of O_2, and excel under specific conditions due to their specific ranges in decay times and absorption and emission spectra. Generally, O_2 sensitive dyes with a long luminescence life-time are more suitable to monitor spatial variation at low O_2 concentrations, while short life-time dyes are more suitable to monitor high O_2 conditions (DeGraff and Demas, 2005; Oguri et al., 2006). Table 1 sums the overall performance and applicability of the three types of O_2 optodes tested in this study. The new IrC optode performs best as a general sensor for luminescence life-time based microscopic O_2 imaging at 0–40% O_2.

4.5. Application in biofilms

In this study, we measured the O_2 dynamics in biofilms at 400× magnification, but the magnification can easily be varied and adapted to the scale relevant for the study object by changing microscope objectives. At lower magnifications (<200×), it was difficult to supply enough excitation light to the optode via the objective, especially with objectives having a large focal distance. In these cases excitation light could be supplied more efficiently externally via two LED's mounted close to the objective.

Planar optodes monitor the O_2 conditions in a defined plane. When an undefined volume of water is between the optode and the object of study, measurements done under steady state conditions will be subject to diffusive smearing. For a more accurate estimate of O_2 production or consumption rates under non steady state conditions an estimate of the water volume is required. In permeable systems convective transport will also alter the O_2 dynamics (Polerecky et al., 2005; Precht et al., 2004). When used as a growth substratum, the biofilm matrix is tightly connected to the optode surface. Therefore, thin-film optodes are ideal for studying the dynamics in spatial O_2 distribution at the biofilm basis as a function of biomass cover and structural heterogeneity.

Our study showed an O_2 penetration depth of ~10–15 μm revealing extremely steep O_2 gradients inside the larger cell aggregates and persistent anoxic conditions inside cell aggregates >25 μm even at elevated flow. Such steep gradients in freshly grown biofilms have been measured before with microelectrodes (DeBeer et al., 1994), while other studies report steep O_2 gradients over >30 μm (e.g. Rasmussen and Lewandowski, 1998; Schramm et al., 1996). The measured gradients represent the outcome of mass transfer limitation and the volume specific consumption rate of O_2. However, in our set-up it is presently difficult to use steady state images of spatial O_2 distribution for simple flux calculations, since the optode measurements integrate effects of heterogeneous biomass distribution and complex mass transfer geometry inside as well as outside of the biofilm.

Even in apparently clean parts of the optode images, it cannot be completely excluded that a very thin biofilm is present, which along with the presence of a diffusive boundary layer can create diffusive smearing. Nevertheless, the imaging of steady state O_2 distribution in biofilms clearly showed the presence of distinct hot spots of activity, which not always link directly to biomass distribution. This is an important result as many studies of biofilms infer distribution of function and microenvironments based on structural analysis with confocal microscopy (Pamp et al., 2009). Our results clearly show that such inference has its limitations as even small differences in biomass geometry and a spatially heterogeneous mass transfer can have profound effects on O_2 levels inside biofilms.

A better estimate of spatial O_2 dynamics could be determined from dynamic imaging of the O_2 distribution over time when turning the flow on and off (Fig. 5). In regions with no bacterial biomass, the O_2 concentration reached its maximum value (6 s) within two measuring points, i.e. over 6 s. The fast response of the optode thus allowed the monitoring of quick changes in O_2 concentration under non steady state conditions.

When maximal O_2 levels were reached upon onset of flow after a period of stagnant conditions, several zones within larger biofilm structures showed a subsequent lowering in O_2 concentration (Fig. 5C), despite the fact that the flow was not changed. We speculate, whether such response reflects an acclimation to a shift from anoxic to oxic conditions. Alternatively, this phenomenon may reflect substrate limitation under stagnant and anoxic conditions resulting in an initial limitation in the first couple of seconds after O_2 became available. In principle, the O_2 depletion rate after stopping the flow reflects the local consumption rates, which can be used to derive kinetic parameters e.g. from a fit of Michaelis–Menten kinetics in the regions where biomass is present. However, in the regions without biomass the O_2 depletion rate will be partly affected by the overlaying volume which is an unknown factor. A study implementing such analyses by the use of O_2 sensitive luminescent nano particles for mapping the spatial distribution and O_2 kinetics in biofilms will be presented elsewhere.

Table 1
General performance of investigated thin-film optodes.

Property	Optode material		
	IrC	Pt-TFPP	Ru-DPP
Brightness	++	+	+
Temperature dependence	Low	Low	High
Sensor homogeneity	++	+	+
Applicability for photosynthetic systems (high pO_2)	+	+	++
Applicability for other systems (low pO_2)	+	++	−
Interference from fluorescence in phototrophic systems	No	Yes, Chl *a*	Yes, cyanobacteria
Photo stability	−	+	+
Commercial availability of the indicator	No	Yes	Yes

5. Conclusion

The new IrC thin-film optodes allow spatial mapping of O_2 in biofilms at a hitherto unreached spatio-temporal resolution. In combination with fluorescent staining of the biomass it is possible to link O_2 distribution and dynamics with biofilm biomass distribution and to detect local variations in O_2 distribution due to biofilm structure and its interaction with flow. It was possible to monitor changes in O_2 consumption around these structures under steady state conditions as well as under non steady state conditions. We show here that O_2 microenvironments inside biofilms are extremely dynamic over spatial scales of 10–20 μm and over time scales of a few seconds. Oxygen conditions in biofilms exhibit dynamic changes in response to flow and substrate conditions and cannot be directly inferred from structural microscopic investigations. Besides biofilm research, this new technique also has a large potential for other research fields where biomass and physiological functions are monitored e.g. in studies of cell and tissue cultures in biotechnology and biomedical research.

Acknowledgements

This study was supported by the Danish Research Council for Technology and Production Sciences (FTP), the Danish Natural Science Research Council (FNU), and the Danish National Advanced Technology Foundation.

Appendix A. Supplementary data

Supplementary data to this article can be found online at doi:10.1016/j.mimet.2011.01.021.

References

Amao, Y., 2003. Probes and polymers for optical sensing of oxygen. Microchim. Acta 143, 1–12.
Bedlek-Anslow, J.M., Hubner, J.P., Carroll, B.F., Schanze, K.S., 2000. Micro-heterogeneous oxygen response in luminescence sensor films. Langmuir 16, 9137–9141.
Borisov, S.M., Klimant, I., 2007. Ultrabright oxygen optodes based on cyclometalated Iridium(III) coumarin complexes. Anal. Chem. 79, 7501–7509.
Carraway, E.R., Demas, J.N., DeGraff, B.A., 1991. Luminescence quenching mechanism for microheterogeneous systems. Anal. Chem. 63, 332–336.
DeBeer, D., Stoodley, P., Roe, F., Lewandowski, Z., 1994. Effects of biofilom structures on oxygen distribution and mass-transport. Biotechnol. Bioeng. 43, 1131–1138.
DeGraff, B.A., Demas, J.N., 2005. Luminescence-based oxygen sensors. Rev. Fluoresc. 125–151.
DeRosa, M.C., Hodgson, D.J., Enright, G.D., Dawson, B., Evans, C.E.B., Crutchley, R.J., 2004. Iridium luminophore complexes for unimolecular oxygen sensors. J. Am. Chem. Soc. 126, 7619–7626.
Eaton, K., Douglas, B., Douglas, P., 2004. Luminescent oxygen sensors: time-resolved studies and modelling of heterogeneous oxygen quenching of luminescence emission from Pt and Pd octaethylporphyrins in thin polymer films. Sens. Act. B Chem. 97, 2–12.
Fenchel, T., Finlay, B., 2008. Oxygen and the spatial structure of microbial communities. Biol. Rev. 83, 553–569.
Gerritsen, H., Sanders, R., Draaijer, A., Ince, C., Levine, Y., 1997. Fluorescence lifetime imaging of oxygen in living cells. J. Fluoresc. 7, 11–15.
Glud, R.N., 2008. Oxygen dynamics of marine sediments. Mar. Biol. Res. 4, 243–289.
Glud, R.N., Ramsing, N.B., Gundersen, J.K., Klimant, I., 1996. Planar optrodes: a new tool for fine scale measurements of two-dimensional O_2 distribution in benthic communities. Mar. Ecol. Prog. Ser. 140, 217–226.
Glud, R.N., Kühl, M., Kohls, O., Ramsing, N.B., 1999. Heterogeneity of oxygen production and consumption in a photosynthetic microbial mat as studied by planar optodes. J. Phycol. 35, 270–279.
Holst, G., Grunwald, B., 2001. Luminescence lifetime imaging with transparent oxygen optodes. Sens. Acta B Chem. 74, 78–90.
Holst, G., Kohls, O., Klimant, I., König, B., Kühl, M., Richter, T., 1998. A modular luminescence lifetime imaging system for mapping oxygen distribution in biological samples. Sens. Acta B Chem. 51, 163–170.
Jimenez, I.M., Kühl, M., Larkum, A.W.D., Ralph, P.J., 2008. Heat budget and thermal microenvironment of shallow-water corals: do massive corals get warmer than branching corals? Limnol. Oceanogr. 53, 1548–1561.
Klimant, I., Wolfbeis, O.S., 1995. Oxygen-sensitive luminescent materials based on silicone-soluble ruthenium diimine complexes. Anal. Chem. 67, 3160–3166.
Klimant, I., Meyer, V., Kühl, M., 1995. Fiberoptic oxygen microsensors, a new tool in aquatic biology. Limnol. Oceanogr. 40, 1159–1165.
Klimant, I., Kühl, M., Glud, R.N., Holst, G., 1997. Optical measurement of oxygen and temperature in microscale: strategies and biological applications. Sens. Acta B Chem. 38, 29–37.
Kühl, M., 2005. Optical microsensors for analysis of microbial communities. Meth. Enzymol. 397, 166–199.
Kühl, M., Polerecky, L., 2008. Functional and structural imaging of phototrophic microbial communities and symbioses. Aquat. Microb. Ecol. 53, 99–118.
Kühl, M., Rickelt, L.F., Thar, R., 2007. Combined imaging of bacteria and oxygen in biofilms. Appl. Environ. Microbiol. 73, 6289–6295.
Liebsch, G., Klimant, I., Frank, B., Holst, G., Wolfbeis, O.S., 2000. Luminescence lifetime imaging of oxygen, pH, and carbon dioxide distribution using optical sensors. Appl. Spectrosc. 54, 548–559.
Oguri, K., Kitazato, H., Glud, R.N., 2006. Platinum octaetylporphyrin based planar optodes combined with an UV-LED excitation light source: an ideal tool for high-resolution O_2 imaging in O_2 depleted environments. Mar. Chem. 100, 95–107.
Pamp, S.J., Sternberg, C., Tolker-Nielsen, T., 2009. Insight into the microbial multicellular lifestyle via flow-cell technology and confocal microscopy. Cytom. A 75A, 90–103.
Polerecky, L., Franke, U., Werner, U., Grunwald, B., de Beer, D., 2005. High spatial resolution measurement of oxygen consumption rates in permeable sediments. Limnol. Oceanogr. Meth. 3, 75–85.
Precht, E., Franke, U., Polerecky, L., Hüttel, M., 2004. Oxygen dynamics in permeable sediments with wave-driven pore water exchange. Limnol. Oceanogr. 49, 693–705.
Rasmussen, K., Lewandowski, Z., 1998. Microelectrode measurements of local mass transport rates in heterogeneous biofilms. Biotechnol. Bioeng. 59, 302–309.
Revsbech, N.P., 2005. Analysis of microbial communities with electrochemical microsensors and microscale biosensors. Meth. Enzymol. 397, 147–166.
Schramm, A., Larsen, L.H., Revsbech, N.P., Ramsing, N.B., Amann, R., Schleifer, K.H., 1996. Structure and function of a nitrifying biofilm as determined by in situ hybridization and the use of microelectrodes. Appl. Environ. Microbiol. 62, 4641–4647.
Wolfbeis, O.S., 2005. Materials for fluorescence-based optical chemical sensors. J. Mater. Chem. 15, 2657–2669.